Binding Motifs of Doubly- and Singly-charged Proton-bound Clusters of $B_{12}F_{12}^{2-}$ and Diaminoalkanes

*Arthur E. Lee[a], Patrick Thomas[a], Courtney Kates[a], Terrance B. McMahon[a], and W. Scott Hopkins[a,b,c]**

[a]Department of Chemistry, University of Waterloo, Waterloo, Ontario, N2L 3G1, Canada

[b]WaterFEL Laboratory, University of Waterloo, Waterloo, Ontario, N2L 3G1, Canada

[c]Centre for Eye and Vision Research, Hong Kong Science Park, New Territories, 999077, Hong Kong.

Corresponding Author Email: shopkins@uwaterloo.ca

Abstract

The complexation of perfluorinated dodecaborate, $B_{12}F_{12}^{2-}$, with protonated diaminoalkanes, $[H_2N(CH_2)_nH_2N]$ (n = 2 – 12), are studied with a combination of infrared multiple photon dissociation (IRMPD) action spectroscopy and ion mobility spectrometry. Singly-charged clusters of the form $[B_{12}F_{12} + H_2N(CH_2)_nH_2N + H]^-$ (n = 2 – 12) and doubly-charged clusters of the form $[2B_{12}F_{12} + H_2N(CH_2)_nH_2N + 2H]^{2-}$ (n = 2 – 12) are observed and characterized experimentally and computationally. For the singly-charged clusters, low-energy structural motifs associated with monodentate and bidentate binding of the diaminoalkane are computed, as well as a conformation involving intramolecular hydrogen bonding between the amino moieties. For the doubly-charged clusters, the doubly-protonated diaminoalkane acts as a tether between two $B_{12}F_{12}^{2-}$ cages. Major product channels of the singly-charged and the doubly-charged species are found to be the formation of $HB_{12}F_{12}^{2-}$ via proton transfer and the loss of $B_{12}F_{12}^{2-}$. The fragmentation of $HB_{12}F_{12}^-$ leads to several secondary products, including $[B_{12}F_{11} + N_2]^-$. Collision cross sections (CCSs) for the singly-charged clusters are reported and the major subpopulation of the gas-phase ensemble for the different singly-charged species is the bidentate conformation.

Introduction

Small boron clusters have been touted for use as therapeutics and as precursors for boron-based nanomaterials.[1–4] In particular, the *closo*-dodecaborate cage species, ($B_{12}X_{12}^{-}$, X = H, F, Cl, Br, I), have attracted interest due to their extraordinary structural and electronic stability, which gives rise to a variety of interesting phenomena and promises application in areas such as energy storage, catalysis, and neutron capture cancer therapy.[5–8] The $B_{12}X_{12}^{2-}$ (X = H, F, Cl, Br, I) dianions have quadruply degenerate g_u symmetry cage-centred HOMOs that are predominantly localised on the boron cage framework..[9] In the case of $B_{12}F_{12}^{2-}$, the negative charge density is delocalized about the surface fluorine atoms, whereas larger halogenated analogues such as $B_{12}I_{12}^{2-}$ have the negative charge delocalization contained within the boron cage.[9] As a consequence of the delocalized excess electron charge density and the charge separation of ion pairs involving $B_{12}X_{12}^{2-}$ species, dodecaborate dianions exhibit relatively weak electrostatic interactions in aqueous solution compared to more common dianions such as SO_4^{2-} and HPO_4^{2-}. Owing to this behaviour, $B_{12}X_{12}^{2-}$ dianions are often referred to as 'weakly coordinating' or 'superweak' anions.[9,10] In the gas phase, however, small dianions such as SO_4^{2-} and HPO_4^{2-} are unstable, whereas $B_{12}X_{12}^{2-}$ species may be readily produced, trapped, and probed.[6,11,12] This exceptional stability enables the study of ionic clusters containing $B_{12}X_{12}^{2-}$.

Previous research of gas-phase clusters containing $B_{12}X_{12}^{2-}$ (X=H, F, Cl, Br, I) demonstrated that the dodecaborate cages are prone to charge-transfer during collision-induced dissociation and IR photodissociation owing to their relatively low oxidation potential.[13] Of the halogenated $B_{12}X_{12}^{2-}$ species, $B_{12}F_{12}^{2-}$ has the lowest oxidation potential.[14] With respect to $B_{12}F_{12}^{2-}$, several studies have explored gas phase clustering interactions with a variety of ligands,[13,15–18] demonstrating that electrostatic interactions are predominantly responsible for cluster

stability.[6,16,17] In their study of $[B_{12}F_{12} + H + N(CH_2CH_3)_3]^-$, Carr *et al.* observed that both proton-transfer and charge-transfer can occur during dissociation,[17] yielding $[HB_{12}F_{12}]^-$ or $B_{12}F_{12}^-$, respectively.[6] Moreover, subsequent HF elimination from $[HB_{12}F_{12}]^-$ can generate the highly electrophilic $[B_{12}F_{11}]^-$ cluster as well as fragments associated with the loss of multiple BF or BF_3 moieties.[19] To further complicate matters, the $[B_{12}F_{11}]^-$ product can react with trace water vapour in the ion trap to induce a reactive cascade whereby HF elimination results in fluorine atoms being replaced by hydroxide groups.[13,19] Interestingly, the analogous $B_{12}Cl_{11}^-$ product was shown *chemically* bind noble gases *via* the superelectrophilic boron site generated via fluorine abstraction.[20,21]

Here, we investigate clusters composed of $B_{12}F_{12}^{2-}$ cages and a series of diaminoalkanes of the form $H_2N(CH_2)_nNH_2$ (n = 2–12). We employ travelling wave ion mobility spectrometry (TWIMS), differential mobility spectrometry (DMS), infrared ion spectroscopy (IRIS), and density functional theory (DFT) to explore how electrostatic interactions, charge-transfer reactions, and incipient chemical bonding influence cluster structures and properties as a function of alkane chain length. Do entropic effects and electrostatic repulsion result in extended geometries, or do hydrogen bonding and dispersion interactions dominate and yield compact geometries? The selected series of diaminoalkanes, which brackets the proton affinity and gas phase basicity of the triethylamine (studied by Carr *et al.*),[17] also enables a more robust investigation of proton-transfer dissociation for the various $[B_{12}F_{12} + H_2N(CH_2)_nNH_2 + H]^-$ and $[2B_{12}F_{12} + H_2N(CH_2)_nNH_2 + 2H]^{2-}$, clusters produced via electrospray ionization.

Experimental Methods

$K_2B_{12}F_{12}$ salt (>97% purity) and linear diaminoalkanes of the form $H_2N(CH_2)_nNH_2$ (n = 2 – 10, 12) (>95% purity) were sourced from Sigma Aldrich, and 1,11-diaminoundecane was

sourced from LGC Standards, Canada. To produce clusters of the form $[B_{12}F_{12} + H_2N(CH_2)_nNH_2 + H]^-$ and $[2B_{12}F_{12} + H_2N(CH_2)_nNH_2 + 2H]^{2-}$, electrospray ionization (ESI) solutions of 200 μM containing the appropriate analytes were prepared separately in a 50:50 methanol and water mixture with 6 % formic acid. This relatively high concentration of formic acid was employed to drive complete protonation of the diaminoalkanes.

High resolution mass spectrometry and collision cross-section (CCS) data was collected using a Waters Synapt G2-Si equipped with a TWIMS cell. The Waters Major Mix was used to generate the CCS calibration curves (Waters Canada, Major Mix IMS/Tof Calibration Kit). As recommended by Gabelica *et al,* calibration curves were created at wave height settings of 36 V, 38 V, and 40 V while maintaining the 500 m/s wave velocity (additional details are provided in the supporting information).[22] The calibration curve (see **Figure S1**) was then used to determine the CCS for each targeted analyte. Sample CCSs were measured with the same wave height settings as used for calibration; TWIMS arrival time distributions exhibited single peaks for all analytes.

Because DMS is sometimes able to separate isomers and conformers that cannot be resolved via other ion mobility techniques,[23] we also probed the $[B_{12}F_{12} + H_2N(CH_2)_nNH_2 + H]^-$ and $[2B_{12}F_{12} + H_2N(CH_2)_nNH_2 + 2H]^{2-}$ clusters using a SCIEX SelexION DMS device. The DMS cell (1 mm gap-height) was mounted between the Turbospray ion source and the sampling orifice of the SCIEX QTRAP 5500 hybrid triple quadrupole linear ion trap mass spectrometer. This instrument has been described in detail elsewhere.[24,25] DMS measurements were recorded at separation voltages (SVs) ranging from SV = 0 – 3000 V in steps of 500 V and from SV = 3000 – 4000 V in 200 V steps, while scanning the compensation voltage (CV) from 3 – 25 V with a step size of 0.25 V. Enhanced product ion (EPI) mode and a collision energy of –10 V was

employed. DMS experiments were conducted at atmospheric pressure in a pure N_2 environment. The optimal CV for ion transmission was measured at each SV to generate dispersion curves for the various clusters.

Infrared ion spectroscopy (IRIS) was also used to probe the structures of the mass-selected $[B_{12}F_{12} + H_2N(CH_2)_nNH_2 + H]^-$ and $[2B_{12}F_{12} + H_2N(CH_2)_nNH_2 + 2H]^{2-}$ clusters. IRIS spectra were recorded at the FELIX free electron laser (FEL) laboratory (Radboud University, Nijmegen, Netherlands) over a wavenumber range of 1300 – 3500 cm^{-1}. Clusters of interest were produced via electrospray ionization and were subsequently isolated within a modified Bruker Amazon quadrupole ion trap mass spectrometer that was interfaced with the FELIX output. This instrument has been described in detail previously.[26,27] Infrared multiple photon dissociation (IRMPD) fragmentation efficiency was tracked as a function of the wavelength of the unattenuated IR-FEL. This form of infrared ion spectroscopy (IRIS), commonly referred to as IRMPD action spectroscopy, is conceptually similar to single photon photodissociation methods (i.e., IRPD).[28]

Computational methods

Candidate geometries for the $B_{12}F_{12}^{2-}$, $[H_2N(CH_2)_nNH_2 + H]^+$ and $[H_2N(CH_2)_nNH_2 + 2H]^{2+}$ monomers were created manually and optimized using the ORCA computational suite.[29] The geometry optimized monomeric species were then combined to create the appropriate $[B_{12}F_{12} + H_2N(CH_2)_nNH_2 + H]^-$ and $[2B_{12}F_{12} + H_2N(CH_2)_nNH_2 + 2H]^{2-}$ clusters, and the CREST algorithm was used to sample the possible cluster conformations.[30] Following conformation sampling, candidate cluster structures were first optimized using the ωb97x-D3/def2-TZVPP method and then refined at the ωb97x-D3BJ/def2-TZVPPD level of theory.[31,32] The level of theory and the basis set was chosen to balance computational resources and accuracy. Frequency calculations were conducted for the geometry optimized clusters to estimate thermochemical

corrections and to generate harmonic vibrational spectra for comparison with the experimental IRIS spectra.

Results and Discussion

Mass Spectrometry Results

High resolution mass spectrometry (HRMS) was used to confirm the identities of the $B_{12}F_{12}^{2-}$ and diaminoalkane clusters. **Figure 1** shows the HRMS spectrum recorded for the singly charged $[B_{12}F_{12} + H_2N(CH_2)_6NH_2 + H]^-$ cluster (*m/z* ~ 475) along with its theoretical isotopic distribution, which arises predominantly from the 1:4 ratio of ^{10}B:^{11}B. Analogous plots for the other singly charged $[B_{12}F_{12} + H_2N(CH_2)_nNH_2 + H]^-$ ($n = 2 – 5, 7 – 12$) clusters, as well as for the doubly charged $[2B_{12}F_{12} + H_2N(CH_2)_nNH_2 + 2H]^{2-}$ ($n = 2 – 12$) clusters are available in the supporting information (**Figures S3–S23)**. In some cases, the presence of other species with more intense MS signals introduced ambiguity to our analyses. For example, the isotopic distribution for the doubly charged $[2B_{12}F_{12} + H_2N(CH_2)_3NH_2 + 2H]^{2-}$ cluster (*m/z* ~ 396) overlapped with that of the $KB_{12}F_{12}^-$ cluster (*m/z* ~ 397), a challenge that was further confounded by the relatively low signal intensity of the $n = 3$ doubly charged cluster. In instances like this, we conducted additional experiments that used the TWIMS cell of our Waters Synapt G2 Si to separate the interfering species from those of interest prior to recording isotopic distributions. TWIMS experiments are discussed in more detail below. The TWIMS-isolated HRMS spectrum for the doubly charged $n = 3$ cluster is shown in **Figure S14**. A possible explanation for the relatively low intensity of this cluster (compared to the $n = 2$ and $n = 4$ analogues) is that singly-protonated 1,3-diaminopropane adopts a stable six-membered ring via intramolecular hydrogen bonding, which disfavours the second protonation and subsequent formation of the doubly charged $n = 3$ cluster. This is

supported by calculations, which indicate that the linear isomer of protonated 1,3-dimainopropane is $\Delta G° = 63$ kJ mol^{-1} higher in energy than the 6-membered ring ground state.

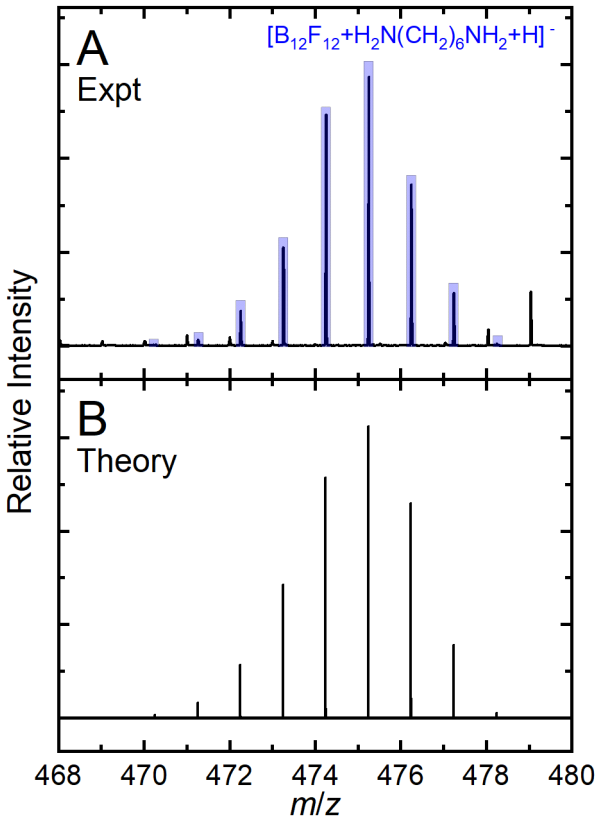

Figure 1. (**A**) The experimental mass spectrum recorded for the $[B_{12}F_{12} + H_2N(CH_2)_6NH_2 + H]^-$ cluster and (**B**) its theoretical isotopic distribution. Experimental *m/z* features associated with the various isotopologues of $[B_{12}F_{12} + H_2N(CH_2)_6NH_2 + H]^-$ are highlighted in blue.

Figure 2 shows the fragmentation mass spectrum of the $[B_{12}F_{12} + H_2N(CH_2)_6NH_2 + H]^-$ cluster as observed following IRMPD and CID. For the most part, both fragmentation techniques generated the same product ions, but with different relative intensities. Two minor features at *m/z* ~394 and *m/z* ~399, for which we do not have a definitive assignment, were observed in CID but not in IRMPD. Based on their masses, we have tentatively provided molecular formulae for these ions (see **Figure 2**). The remaining product ions were assigned to a variety of boron and

fluorine containing species, many of which had been identified previously in the $[B_{12}F_{12} + N(CH_2CH_3)_3 + H]^-$ study by Carr *et al*.[33] The most prominent product ion observed is $B_{12}F_{11}^-$ (*m*/*z* ~339), which is produced via HF elimination from $HB_{12}F_{12}^-$ (*m*/*z* ~359), which itself is a product of proton-transfer dissociation of the parent $[B_{12}F_{12} + H_2N(CH_2)_6NH_2 + H]^-$ cluster. We note that very little $B_{12}F_{12}^{2-}$ (*m*/*z* ~179) is produced via CID or IRMPD, indicating that the proton transfer dissociation pathway is the dominant product channel. Loss of HF from $HB_{12}F_{12}^-$ to generate the (very reactive) $B_{12}F_{11}^-$ cluster results in further fragmentation of the boron cage cluster (*e.g.*, successive F losses) as well as reactions with the background N_2 gas to form the $[B_{12}F_{11} + N_2]^-$ cluster (*m*/*z* ~367). We also see formation of $[B_{12}F_{11} + Ar]^-$ (*m*/*z* ~379), which arises due to reaction with the $Ar_{(g)}$ that is used for CID. Reaction of $B_{12}X_{11}^-$ (X = halogens, CN) anions with inert gases was first reported by Rohdenburg *et al*.,[34] who demonstrated binding of Kr and Xe to the superelectrophilic site of $B_{12}Cl_{11}^-$ (produced via CID of $B_{12}Cl_{12}^{2-}$). With regard to the singly charged $[B_{12}F_{12} + H_2N(CH_2)_nNH_2 + H]^-$ ($n = 2 – 12$) and the doubly charged $[2B_{12}F_{12} + H_2N(CH_2)_nNH_2 + 2H]^{2-}$ ($n = 2 – 12$) clusters studied here, the fragmentation behavior shown in **Figure 2** is relatively consistent across the entire series (see **Figures S35 – S55**). To further confirm the identity of the $[B_{12}F_{11} + N_2]^-$ cluster, we conducted CID experiments for a few test cases with the source of N_2 (*i.e.*, the TWIMS cell) turned off. Doing so resulted in the disappearance of the $[B_{12}F_{11} + N_2]^-$ peak from the mass spectrum.

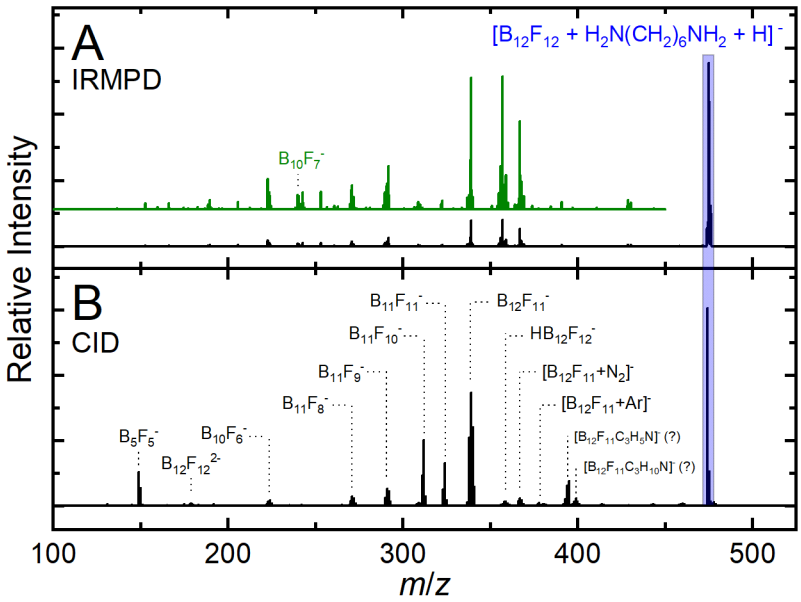

Figure 2. Fragment mass spectra observed for $[B_{12}F_{12} + H_2N(CH_2)_6NH_2 + H]^-$ ($m/z \sim 475$) following (**A**) IRMPD and (**B**) CID. The parent ion is highlighted in blue. Tentative assignments are provided for the features at $m/z \sim 394$ and $m/z \sim 399$. The remaining mass features are assigned based on the reference 33.

Computational Results

To explore the structures and properties of the $[B_{12}F_{12} + H_2N(CH_2)_nNH_2 + H]^-$ ($n = 2 – 12$) and $[2B_{12}F_{12} + H_2N(CH_2)_nNH_2 + 2H]^{2-}$ ($n = 2 – 12$) clusters, we first conducted a detailed computational study. CREST sampling followed by DFT optimization yields three structural motifs for the singly-charged species, $[B_{12}F_{12} + H_2N(CH_2)_nNH_2 + H]^-$ ($n = 2 – 12$), based on the geometry of the diaminoalkane: (*i*) monodentate binding, (*ii*) bidentate binding, and (*iii*) proton-bound ring structures. **Figure 3A – C** shows examples of these structural motifs for the $[B_{12}F_{12} + H_2N(CH_2)_6NH_2 + H]^-$ cluster along with relative Gibbs energies. In this case, the lowest energy structural motif is that of the proton-bound ring structure, which lies *ca.* 30 kJ mol^{-1} below the monodentate and bidentate structures. Calculations indicate that for the singly-charged species

with $n \leq 8$, the proton-bound ring structural motif is the preferred geometry. However, for $n \geq 9$ the isomeric forms re-order energetically and the bidentate motif becomes the favoured geometry. **Figure S2** plots the relative energies of the structural motifs of the $[B_{12}F_{12} + H_2N(CH_2)_nNH_2 + H]^-$ clusters as a function of n.

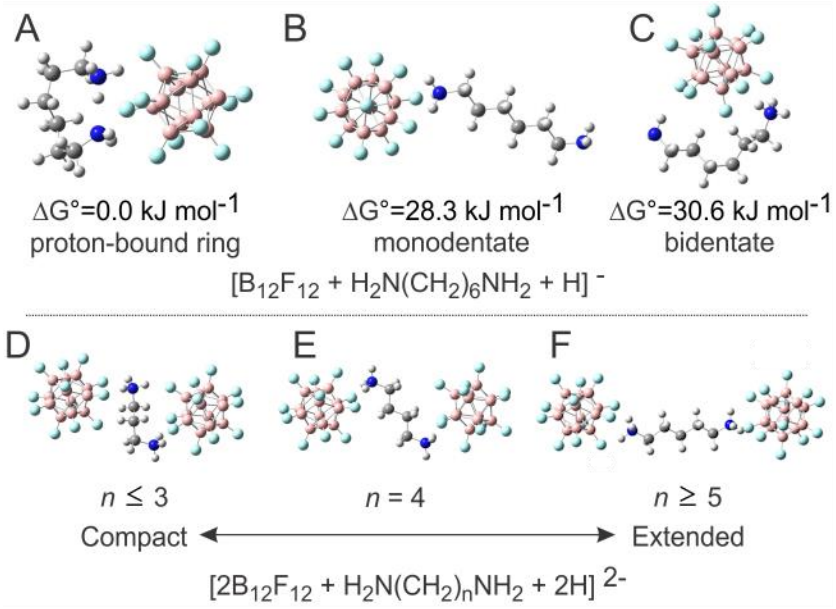

Figure 3. (**Top**) Computed geometries of the $[B_{12}F_{12} + H_2N(CH_2)_6NH_2 + H]^-$ cluster: (**A**) proton-bound ring structure, (**B**) monodentate-bound structure, and (**C**) bidentate-bound structure. Calculated relative Gibbs energies for the three isomers are given in kJ mol^{-1}. (**Bottom**) Computed geometries of the $[2B_{12}F_{12} + H_2N(CH_2)_nNH_2 + 2H]^{2-}$ (n = 3, 4, 5) clusters. (**D**) The structure of the n = 3 doubly-charged cluster is representative of the ground state of those containing diaminopropane and diaminoethane species. (**E**) The structure of the n = 4 doubly-charged cluster. (**F**) The structure of the n = 5 doubly-charged cluster is representative of the ground state of those containing diaminopentane and longer chain species.

Figures 3D – F show the computed global minima for the $[2B_{12}F_{12} + H_2N(CH_2)_nNH_2 + 2H]^{2-}$ (n = 3 – 5) clusters. Calculations indicate compact geometries for clusters with $n \leq 3$ and extended

structures for clusters with $n \geq 4$. Interestingly, for clusters with $n \leq 3$, the extended geometries were not stable minima and collapsed into the compact form upon geometry optimization (*i.e.*, extended geometries were not stable, higher energy conformers). This behavior is likely driven by four factors: (*i*) the Coulombic repulsion of the $B_{12}F_{12}^{2-}$ cages, (*ii*) the Coulombic repulsion of the ammonium groups of the doubly-protonated diaminoalkane, (*iii*) the entropy of the doubly-protonated diaminoalkane chain, and (*iv*) the attractive forces (*i.e.*, Coulombic and hydrogen-bonding) between the $B_{12}F_{12}^{2-}$ cages and the ammonium groups. For the short-chain diaminoalkanes ($n = 2, 3$), the distance between the $B_{12}F_{12}^{2-}$ cages in the compact and (hypothetical) extended forms is not significantly different so factors (*i*) and (*ii*) will be relatively similar in both cases by virtue of the $1/r^2$ dependence of Coulombic interactions. Moreover, the conformational space for these short-chain diaminoalkanes is relatively small and restricting their geometry in the compact cluster form has a relatively minor impact on the system entropy. However, as shown in Figure 3 for the case of the $n = 3$ cluster, the proximity of the $B_{12}F_{12}^{2-}$ cages to both ammonium groups of the short-chain species yields additional stabilizing attractive interactions. The balance of these driving forces leads to the adoption of compact structures for the short chain species. In contrast, the stabilization afforded by introducing additional hydrogen bonding does not overcome the entropic penalty of restricted geometry in the clusters that contain longer chain diaminoalkanes. This behaviour is reflected in the computed gas phase basicity and proton affinity for the diaminoalkanes (see **Table S4** and **S5**); gas phase basicities, for example, increase from 507 kJ mol^{-1} to 828 kJ mol^{-1} across the range $n = 2 – 12$.

The computed binding energies for the proton-transfer dissociation process $[B_{12}F_{12} + H_2N(CH_2)_nNH_2 + H]^- \rightarrow HB_{12}F_{12}^- + H_2N(CH_2)_nNH_2$ ($n = 2, 6, 12$) are provided in **Table 1** and energies for the remaining analogous $[B_{12}F_{12} + H_2N(CH_2)_nNH_2 + H]^-$ clusters are provided in

Table S7. Standard Gibbs binding energies for the lowest energy conformations range from *ca*. 160 – 210 kJ mol^{-1}. As expected, the trend in binding energy as a function of *n* mirrors that of the relative conformer energies. In comparison, dissociation energies of the singly-charged clusters to yield $B_{12}F_{12}^{2-}$ (*i.e.*, direct dissociation without proton transfer) are significantly higher in energy (see **Table S8**), ranging from 491 – 576 kJ mol^{-1}. This result accords with experiment, where the formation of $B_{12}F_{12}^{2-}$ was observed to be a (very) minor product channel via CID and IRMPD for all clusters. Charge-transfer dissociation to yield $B_{12}F_{12}^{-}$ was not observed.

Table 1. Computed binding energies for $[B_{12}F_{12} + H_2N(CH_2)_nNH_2 + H]^-$ dissociating to $H_2N(CH_2)_nNH_2 + HB_{12}F_{12}^-$ products for $n = 2$, 6, 12. Electronic energies (ΔE_{elec}), zero-point corrected energies (ΔE_{zpe}), enthalpies (ΔH), and standard Gibbs energies ($\Delta G°$) are reported in kJ mol^{-1}, and entropy (ΔS) is reported in units of kJ mol^{-1} K^{-1}.

Cluster	ΔE_{elec}	ΔE_{zpe}	ΔH	ΔS	$\Delta G°$
Monodentate conformation					
$n = 2$	244.2	223.6	223.1	53.7	169.3
$n = 6$	243.9	224.0	223.4	56.9	166.5
$n = 12$	243.0	223.4	222.5	58.6	163.9
Bidentate conformation					
$n = 2$	244.2	223.5	223.0	53.8	169.2
$n = 6$	248.0	226.0	226.2	61.9	164.3
$n = 12$	278.6	255.2	256.1	69.2	186.9
Proton-bound ring conformation					
$n = 2$	256.4	236.6	236.4	55.0	181.4
$n = 6$	295.0	272.3	273.0	63.8	209.2
$n = 12$	278.3	251.5	182.8	254.1	182.8

The computed binding energies for the doubly-charged $[2B_{12}F_{12} + H_2N(CH_2)_nNH_2 + 2H]^{2-}$ (n = 2 – 12) clusters are provided in **Table 2**. As was the case with the singly-charged species, the proton-transfer product channel (leading to formation of $HB_{12}F_{12}^-$) is thermodynamically favoured over the $B_{12}F_{12}^{2-}$ product channel. However, we find that the gap between these thresholds diminishes substantially with increasing length of the diaminoalkane chain; for the n = 2 cluster, the energy gap between thresholds is $\Delta E = 164$ kJ mol^{-1}, whereas for n = 12 the gap is $\Delta E = 8$ kJ mol^{-1}. This stabilization of the $B_{12}F_{12}^{2-}$ product channel relative to the $HB_{12}F_{12}^-$ product channel is reflected in the CID fragmentation spectra, which show significantly more intensity in the $B_{12}F_{12}^{2-}$ mass channel for clusters containing longer diaminoalkanes (0.3% of total ion signal for n = 2 versus 4.7% of total ion signal for n = 12). In comparison, a similar analysis of the singly-charged $[B_{12}F_{12} + H_2N(CH_2)_nNH_2 + H]^-$ clusters reveals that the energy gap between product thresholds diminishes from $\Delta E = 66$ kJ mol^{-1} to $\Delta E = 28$ kJ mol^{-1} across the n = 2 – 12 series, and the $B_{12}F_{12}^{2-}$ ion signal observed in CID increases from 0.2% to 2.0% of total ion signal, accordingly.

Table 2. Computed binding energies for $[2B_{12}F_{12} + H_2N(CH_2)_nNH_2 + 2H]^{2-}$ dissociating to: (I.) $[B_{12}F_{12} + H_2N(CH_2)_nNH_2 + H]^- + HB_{12}F_{12}^-$ and (II.) $[B_{12}F_{12} + H_2N(CH_2)_nNH_2 + 2H]^0 + B_{12}F_{12}^{2-}$ products for $n = 2$, 6, 12. Electronic energies (ΔE_{elec}), zero-point corrected energies (ΔE_{zpe}), enthalpies (ΔH), and standard Gibbs energies ($\Delta G°$) are reported in kJ mol^{-1} , and entropy (ΔS) is reported in units of kJ mol^{-1} K^{-1}.

Cluster	ΔE_{elec}	ΔE_{zpe}	ΔH	ΔS	$\Delta G°$
$HB_{12}F_{12}^-$ Formation					
$n = 2$	199.0	180.5	188.4	85.2	103.2
$n = 6$	192.1	172.5	171.6	62.5	109.1
$n = 12$	229.8	211.7	217.6	81.4	136.2
$B_{12}F_{12}^{2-}$ Formation					
$n = 2$	345.4	341.2	346.8	79.6	267.2
$n = 6$	219.8	220.9	216.5	49.9	166.6
$n = 12$	202.8	207.2	209.2	65.2	144.0

Ion Mobility Spectrometry Results

To investigate the possibility of multiple isomeric sub-populations in the gas phase ensemble, we conducted TWIMS experiments for the $[B_{12}F_{12} + H_2N(CH_2)_nNH_2 + H]^-$ and $[2B_{12}F_{12} + H_2N(CH_2)_nNH_2 + 2H]^{2-}$ clusters for $n = 2 – 12$. Collision cross-sections (CCSs) for all ions measured are tabulated in the supporting information (**Table S2**). The $[B_{12}F_{12} + H_2N(CH_2)_nNH_2 + H]^-$ clusters are found to have CCSs that range from 180 $Å^2$ ($n = 2$) to 218 $Å^2$ ($n = 12$), with a relatively linear increase in CCS values as a function of the length of the diaminoalkane chain (see **Figure 4**). We do not resolve multiple features in our TWIMS experiments. However, we note that the linear trend of increasing CCS with increasing size of

diaminoalkane chain length deviates slightly at $n = 10$, which also exhibits a significantly broader arrival time distribution than the other clusters. This is approximately the same region that calculations predict there to be an energetic reordering of the low-energy structural motifs; the proton-bound ring structure being favoured for $n \leq 8$ and the bidentate structure favoured for $n \geq 9$. Overlayed on Figure 4 are CCSs for the various cluster isomers, which we computed using MobCal-MPI.[35] Because MobCal-MPI is not parameterized to include boron, we employed the force field parameters for sp^3 hybridized carbon to approximate the boron parameters while maintaining the DFT-calculated cluster geometries and partial charges. Since this treatment will introduce minor systematic errors to the calculations, one is cautioned against over-interpreting the resulting CCS values. However, given that the fluorinated surface of the $B_{12}F_{12}$ cages will predominantly participate in gas phase collisions (rather than the boron cage framework) and that F is parameterized within MobCal-MPI, we anticipate semi-quantitative agreement for the relative CCS trends of the cluster structural motifs owing to the internal consistency of our computational approach. When comparing the computed CCSs to those measured experimentally, we find relatively good agreement with the trends for the proton-bound ring and bidentate motifs. Considered collectively, our TWIMS measurements and supporting CCS calculations suggest that there may be multiple isomers present for the longer chain species, which accords with expectations based on the relative energies of DFT-computed cluster conformers.

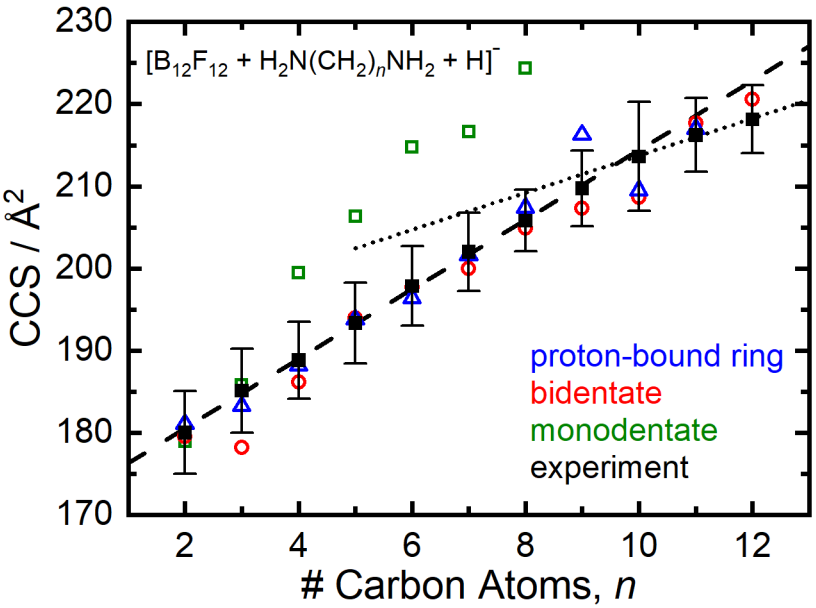

Figure 4. (**Black**) Measured CCSs for the $[B_{12}F_{12} + H_2N(CH_2)_nNH_2 + H]^-$ ($n = 2 – 12$) clusters. Error bars indicate the full width at half maximum for the arrival time distributions. The dashed line shows a linear trend that was fit to the $n = 2 – 9$ clusters. The dotted line shows a linear trend that was fit to the $n = 10 – 12$ clusters. Computed CCS values for the (**green**) monodentate, (**red**) bidentate, and (**blue**) proton-bound ring structures.

To explore further the isomeric composition of the gas phase cluster ensembles, we measured the differential ion mobility behaviour of each cluster. DMS has been shown to resolve isomeric features that cannot be resolved via TWIMS, although care must be taken to account for artefacts associated with fragmentation of larger cluster species.[23,36,37] **Figure 5** shows the DMS ionograms measured for the $[B_{12}F_{12} + H_2N(CH_2)_nNH_2 + H]^-$ ($n = 4$, 10) clusters. Overlayed in red are the ionograms measured for the $[2B_{12}F_{12} + H_2N(CH_2)_nNH_2 + 2H]^{2-}$ ($n = 4$, 10) clusters, which fragment in the post-DMS transfer ion optics to generate the singly-charged analogues (observed at CV ≈ 13 V). Analogous plots for the other clusters studied are provided in the supplementation information (see **Figures S24-34**). Given that the feature at CV = 13 V in figure 5A is associated

with fragmentation of the $[2B_{12}F_{12} + H_2N(CH_2)_4NH_2 + 2H]^{2-}$ cluster, the single remaining feature observed in the ionogram of $[B_{12}F_{12} + H_2N(CH_2)_4NH_2 + H]^-$ indicates that this cluster exhibits a single structural motif in its gas phase ensemble under the given experimental conditions (see **Figure 5A**). In contrast, the ionogram of $[B_{12}F_{12} + H_2N(CH_2)_{10}NH_2 + H]^-$ exhibits two features after accounting for fragmentation of the $[2B_{12}F_{12} + H_2N(CH_2)_{10}NH_2 + 2H]^{2-}$ cluster (which generates the singly-charged analogue and $HB_{12}F_{12}^-$; see **Figure 5B**). In fact, the second, lower intensity feature is visible in all $[B_{12}F_{12} + H_2N(CH_2)_nNH_2 + H]^-$ ($n = 6 - 12$) ionograms (**see Figures S28-34**), suggesting that two isomeric forms may be present in the gas phase ensembles of the larger clusters. Unfortunately, both features exhibited the same fragmentation behaviour and precursor ion scans, and cannot conclusively assigned to specific cluster geometries. Nevertheless, given our computational results, we favour the larger peak at CV ≈ 7 V to be associated with the proton-bound ring structure and the peak at CV ≈ 22 V to be associated with the bidentate structure.

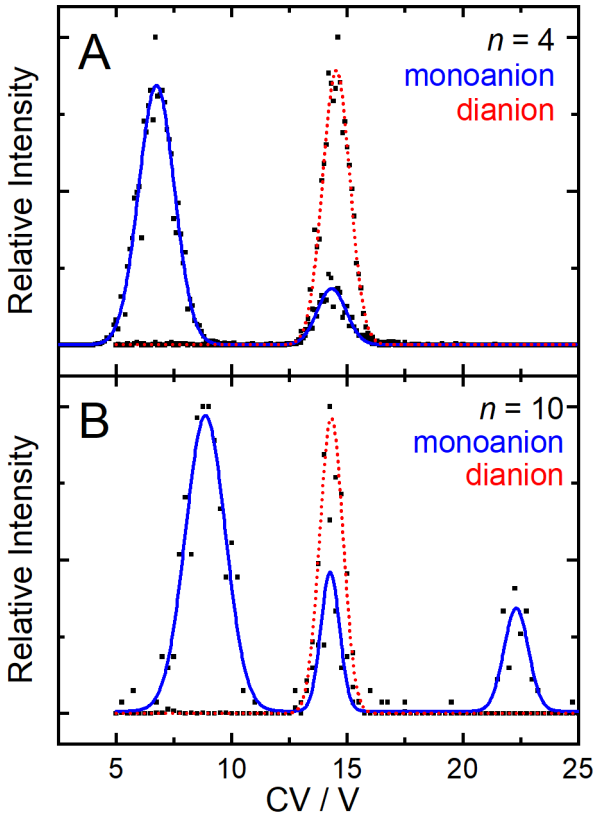

Figure 5. Ionograms of (**A, blue**) $[B_{12}F_{12} + H_2N(CH_2)_4NH_2 + H]^-$ and (**A, red**) $[2B_{12}F_{12} + H_2N(CH_2)_4NH_2 + 2H]^{2-}$ measured at SV = 3800 V in a pure N_2 environment. (**B, blue**) Ionograms of $[B_{12}F_{12} + H_2N(CH_2)_{10}NH_2 + H]^-$ and (**B, red**) $[2B_{12}F_{12} + H_2N(CH_2)_{10}NH_2 + 2H]^{2-}$ measured at SV = 3800 V in a pure N_2 environment. Ionograms for the other clusters measured at the same SV are provided in the supporting information (**Figure S24-34**).

Infrared Ion Spectroscopy (IRIS) Results

As a final exploration of cluster structure, IRIS experiments were performed on the mass-selected $[B_{12}F_{12} + H_2N(CH_2)_nNH_2 + H]^-$ and $[2B_{12}F_{12} + H_2N(CH_2)_nNH_2 + 2H]^{2-}$ ($n = 2 – 12$) clusters. Figure 6 provides a comparison of the experimental spectrum recorded for the $[B_{12}F_{12} + H_2N(CH_2)_{12}NH_2 + H]^-$ cluster along with the computed spectra for the monodentate, bidentate, and proton-bound ring isomers. Table S9 provides assignment of the fundamental

vibrational bands based on the computational results for the singly-charged clusters. The spectral intensity near 3,300 cm^{-1} demonstrates the presence of the bidentate and/or the proton-bound ring structure since the monodentate isomer does not absorb in this region. Similarly, the intensity observed near 2,700 cm^{-1} demonstrates the presence of the proton-bound ring structure since only this conformer absorbs at wavenumbers in the 2,500 – 2,900 cm^{-1} region. That this band is not as sharp and intense as predicted by theory stems from the fact that it is associated with the shared proton vibration of the protonated 1,12-diaminododecane moiety; shared protons are notoriously anharmonic and often exhibit broad bands of relatively low intensity.[38,39] IR absorption (and subsequent cluster dissociation) across this region as a function of diaminoalkane chain length indicates that the proton-bound ring structure is present for all clusters sizes. Unfortunately, owing to spectral congestion there are no isolated diagnostic vibrational bands for either of the other two motifs (*viz*. monodentate, bidentate). As a note for completeness, the doubly-charged $[2B_{12}F_{12} + H_2N(CH_2)_{12}NH_2 + 2H]^{2-}$ ($n = 2 – 12$) clusters, for which there was computed only a singly low-energy isomer for each cluster size, exhibited relatively sparse spectra that aligned very well with computed harmonic absorption spectra (see Figures S67-69).

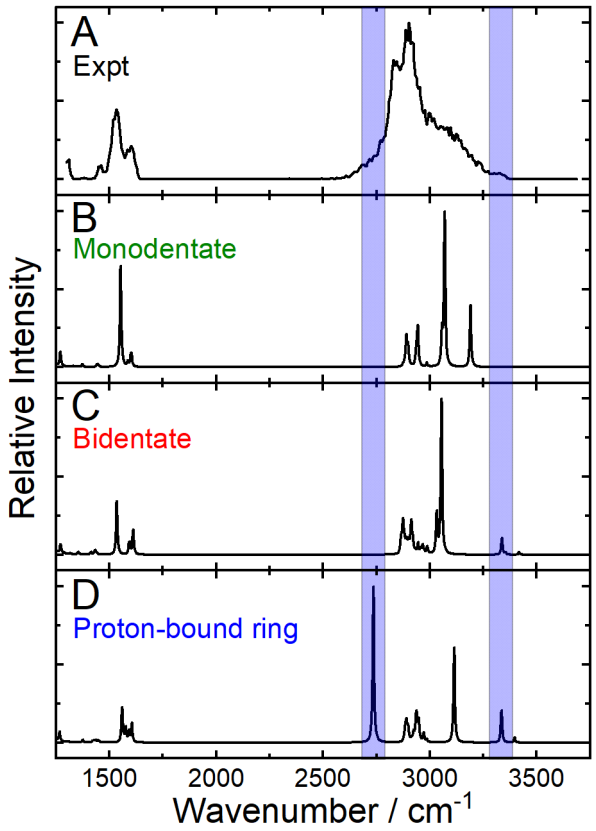

Figure 6. (**A**) The experimental IRIS spectrum for the $[B_{12}F_{12} + H_2N(CH_2)NH_2 + H]^-$ cluster and the computed spectra of the (**B**) monodentate, (**C**) bidentate, and (D) proton-bound ring isomers. The intensity observed near 2,700 cm^{-1} demonstrates that the proton-bound-ring structure is present in the probed ensemble.

Interestingly, different band intensities were observed in spectra from different IRMPD product channels of the same parent molecule. For example, the spectra observed in the $m/z \sim 358$ ($HB_{12}F_{12}^-$) and $m/z \sim 339$ ($B_{12}F_{11}^-$) product channels of the $[B_{12}F_{12} + H_2N(CH_2)_{12}NH_2 + H]^-$ cluster are markedly different. For example, the m/z 339 channel exhibits relatively narrow bands with substantially more intensity in the >2,900 cm^{-1} region than in the *ca*. 1,500 cm^{-1} region, whereas the m/z 358 channel exhibits relatively broad bands with substantially higher intensity in the *ca*. 1,500 cm^{-1} region than at >2,900 cm^{-1} (see **Figure S70**. This behaviour can likely be

attributed to the power dependence of the processes to produce $HB_{12}F_{12}^-$ and $m/z \sim 339$ $B_{12}F_{11}^-$. Because $B_{12}F_{11}^-$ is produced via HF loss from $HB_{12}F_{12}^-$, excitation via the high absorption cross-section bands in the 2,900 – 3,200 cm^{-1} region leads to a reaction cascade from the parent to $HB_{12}F_{12}^-$ to $B_{12}F_{11}^-$, thus artificially diminishing the band intensity in the $m/z \sim 358$ channel and inflating that observed in the $m/z \sim 339$ ($B_{12}F_{11}^-$) product channel. We attempted to confirm this with a power study at the FELIX facility, but results were inconclusive because the clusters were too insensitive to fragmentation across the range of attenuations offered at the facility (*i.e.*, good signal-to-noise was observed only with the unattenuated beam).

Conclusions

Electrospray ionization of solutions containing $B_{12}F_{12}^{2-}$ and diaminoalkanes of the form $H_2N(CH_2)_nNH_2$ ($n = 2 – 12$) yields $[B_{12}F_{12} + H_2N(CH_2)_nNH_2 + H]^-$ and $[2B_{12}F_{12} + H_2N(CH_2)_nNH_2 + 2H]^{2-}$ ($n = 2 – 12$) clusters. Fragmentation of these clusters occurs via: (*i*) proton-transfer to yield $HB_{12}F_{12}^-$ and, to a minor extent, (*ii*) direct dissociation to yield $B_{12}F_{12}^{2-}$. The $HB_{12}F_{12}^-$ product generated via proton-transfer product can undergo further fragmentation to generate smaller clusters associated with loss of BF and BF_3, or by HF elimination to yield the highly electrophilic $B_{12}F_{11}^-$ species, which can subsequently react with trace water vapor or inert gases in the ion trap to form species such as $[B_{12}F_{11} + N_2]^-$ and $[B_{12}F_{11}+Ar]^-$. The computed standard Gibbs energy for the formation of $HB_{12}F_{12}^-$ from the $[2B_{12}F_{12} + H_2N(CH_2)_nNH_2 + 2H]^{2-}$ ($n = 2 – 12$)species is 103.2 kJ mol^{-1} at $n = 2$, increasing to 136.2 kJ mol^{-1} at $n = 12$. In contrast, the standard Gibbs energy for the loss of $B_{12}F_{12}^{2-}$ from these species is 267 kJ mol^{-1} at $n = 2$, decreasing to 144 kJ mol^{-1} at $n = 12$. Similar trends are observed for the $[B_{12}F_{12} + H_2N(CH_2)_nNH_2 + H]^-$ ($n = 2 – 12$) species. The computed Gibbs energies align with the observation that $HB_{12}F_{12}^-$ (and secondary products formed from $HB_{12}F_{12}^-$) are the major

product ions observed for the $[B_{12}F_{12} + H_2N(CH_2)_nNH_2 + H]^-$ and $[2B_{12}F_{12} + H_2N(CH_2)_nNH_2 + 2H]^{2-}$ ($n = 2 – 12$) clusters.

Calculations of the $[2B_{12}F_{12} + H_2N(CH_2)_nNH_2 + 2H]^{2-}$ ($n = 4 – 12$) clusters indicate that they adopt an extended geometry whereby the dodecaborate cages are maximally separated. For smaller chain lengths, a more compact structure is adopted to maximize the Coulombic attraction between the $B_{12}F_{12}^{2-}$ cages and the ammonium groups of the doubly-protonated diaminoalkane. For the $[B_{12}F_{12} + H_2N(CH_2)_nNH_2 + H]^-$ ($n = 2 – 12$) species, three binding motifs were identified: (*i*) monodentate binding of the diaminoalkane, (*ii*) bidentate binding, and (*iii*) clusters in which the diaminoalkane adopted a proton-bound ring structure. To investigate further the possibility that multiple isomers are present in the gas-phase ensemble, TWIMS and DMS experiments were conducted. The $[B_{12}F_{12} + H_2N(CH_2)_nNH_2 + H]^-$ ($n = 2 – 12$) species were found to have CCS values ranging from 180 Å^2 ($n = 2$) to 218 Å^2 ($n = 12$), with a relatively linear increase in CCS as a function of the diaminoalkane chain length. This linear trend of increasing CCS with increasing diaminoalkane chain length deviates at $n = 10$, suggesting that there may be multiple conformations within the probed ensemble and that the dominant binding motif is different for longer chain lengths than shorter chain lengths. DMS experiments were undertaken to resolve the cluster conformers. For $[B_{12}F_{12} + H_2N(CH_2)_nNH_2 + H]^-$ ($n = 2 – 4$), two features are observed in the respective DMS ionograms, with the feature to higher CV coinciding with that of the $[B_{12}F_{12} + H_2N(CH_2)_nNH_2 + 2H]^{2-}$ ($n = 2 – 4$) analogue. In other words, the $[B_{12}F_{12} + H_2N(CH_2)_nNH_2 + 2H]^{2-}$ ($n = 2 – 4$) analogue fragments post-DMS-separation to generate $HB_{12}F_{12}^-$ and the corresponding $[B_{12}F_{12} + H_2N(CH_2)_nNH_2 + H]^-$ ($n = 2 – 4$) species. For the $[B_{12}F_{12} + H_2N(CH_2)_nNH_2 + H]^-$ ($n = 5 – 12$) species, three features are observed in their respective DMS ionograms, only one of which corresponds to fragmentation of the

$[B_{12}F_{12} + H_2N(CH_2)_nNH_2 + 2H]^{2-}$ (n = 5 – 12) analogues. The remaining two ionogram features are tentatively assigned to the proton-bound ring motif (larger feature) and the bidentate motif (smaller feature) based on computed relative energies.

To further probe the structures of the $[B_{12}F_{12} + H_2N(CH_2)_nNH_2 + H]^-$ and $[2B_{12}F_{12} + H_2N(CH_2)_nNH_2 + 2H]^{2-}$ (n = 2 – 12) clusters, IRIS experiments were conducted. A vibrational band observed at *ca*. 2,700 cm^{-1} provided evidence for the presence of the proton-bound ring motif for all $[B_{12}F_{12} + H_2N(CH_2)_nNH_2 + H]^-$ (n = 2 – 12) species. The bidentate structures, which based on calculations are also expected to be present in the probed ensembles, yield computed spectra that accord with other features in the experimental IRIS spectra. However, the same is true of the higher energy monodentate structures, so we are unable to conclusively discount their presence. The $[2B_{12}F_{12} + H_2N(CH_2)_nNH_2 + 2H]^{2-}$ (n = 2 – 12) clusters, for which calculations indicate the presence of a single low-energy conformer for all chain lengths, exhibited relatively sparse spectra that aligned well with those predicted by DFT. Introducing DMS mobility-selection prior to IR interrogation could enable some degree of spectral deconvolution in the future. Given the variation in electron density distribution down the period for the halogenated $B_{12}X_{12}^{2-}$ species, it would also be interesting to explore whether the analogous $B_{12}X_{12}^{2-}$ (X = H, Cl, Br, I) clusters exhibit similar behaviour to that of the $B_{12}F_{12}^{2-}$ clusters studied here.

Associated content

Supporting Information

Supporting information provides the information regarding the CCS calculation and CCSs for the calibrant ions and the targeted analytes. In addition, the supporting information includes the ionograms for both singly charged and doubly charged species, IRIS spectra of the singly charged

and the doubly charged diaminoalkane-$B_{12}F_{12}^{2-}$ clusters, and the IRMPD-CID comparisons for each measured species. Computed structure of each compound can be accessed through the following link: http://dx.doi.org/10.19061/iochem-bd-6-419

AUTHOR INFORMATION

Corresponding Author

W. Scott Hopkins (email: shopkins@uwaterloo.ca)

The authors declare no competing financial interests.

Author Contributions

AEL performed experiments and supporting calculations. PT assisted with the IRIS experiments and CK assisted with the DMS experiments. WSH and TBM were responsible for conceptualization and funding, and they aided in the interpretation of results and manuscript preparation.

ACKNOWLEDGMENTS

The authors would like to acknowledge the high-performance computing support from Digital Research Alliance of Canada (The Alliance). WSH would like to acknowledge the financial support provided by the Natural Sciences and Engineering Research Council (NSERC) of Canada in the form of Discovery, Engage, and Alliance grants, and the InnoHK initiative and the Hong Kong Special Administrative Region Government. TBM would like to acknowledge the financial support provided by the Natural Sciences and Engineering Research Council (NSERC) of Canada in the form of Discovery grant. Also, we would like to acknowledge the help from Prof. Jon Martens and the staffs from the FELIX facility in Radboud University.

References

(1) Barba-Bon, A.; Salluce, G.; Lostalé-Seijo, I.; Assaf, K. I.; Hennig, A.; Montenegro, J.; Nau, W. M. Boron Clusters as Broadband Membrane Carriers. *Nature* **2022**, *603* (7902), 637–642. https://doi.org/10.1038/s41586-022-04413-w.

(2) Murphy, N.; McCarthy, E.; Dwyer, R.; Farràs, P. Boron Clusters as Breast Cancer Therapeutics. *J. Inorg. Biochem.* **2021**, *218*, 111412. https://doi.org/10.1016/j.jinorgbio.2021.111412.

(3) An, L.; Yu, Y.; Cai, Q.; Mateti, S.; Li, L. H.; Chen, Y. I. Hexagonal Boron Nitride Nanosheets: Preparation, Heat Transport Property and Application as Thermally Conductive Fillers. *Prog. Mater. Sci.* **2023**, *138*, 101154. https://doi.org/10.1016/j.pmatsci.2023.101154.

(4) Rasul, M. G.; Kiziltas, A.; Arfaei, B.; Shahbazian-Yassar, R. 2D Boron Nitride Nanosheets for Polymer Composite Materials. *Npj 2D Mater. Appl.* **2021**, *5* (1), 1–18. https://doi.org/10.1038/s41699-021-00231-2.

(5) Udovic, T. J.; Matsuo, M.; Unemoto, A.; Verdal, N.; Stavila, V.; Skripov, A. V.; Rush, J. J.; Takamura, H.; Orimo, S. Sodium Superionic Conduction in $Na_2B_{12}H_{12}$. *Chem Commun* **2014**, *50* (28), 3750–3752. https://doi.org/10.1039/C3CC49805K.

(6) Jenne, C.; Keßler, M.; Warneke, J. Protic Anions $[H(B_{12}X_{12})]^-$ (X=F, Cl, Br, I) That Act as Brønsted Acids in the Gas Phase. *Chem. – Eur. J.* **2015**, *21* (15), 5887–5891. https://doi.org/10.1002/chem.201500034.

(7) Shmalko, A. V.; Anufriev, S. A.; Timofeev, S. V.; Sivaev, I. B.; Bregadze, V. I. Synthesis of New Fluoro Derivatives of O-Carborane $[3\text{-F-}7,8\text{-}C_2B_9H_{11}]^-$, $3,6\text{-}F_2\text{-}1,2\text{-}C_2B_{10}H_{10}$, and [6,6′-

F_2-3,3′-Co(1,2-$C_2B_9H_{10})_2]^-$. *Russ. Chem. Bull.* **2024**, *73* (1), 146–152. https://doi.org/10.1007/s11172-024-4126-9.

(8) Soloway, A. H.; Tjarks, W.; Barnum, B. A.; Rong, F.-G.; Barth, R. F.; Codogni, I. M.; Wilson, J. G. The Chemistry of Neutron Capture Therapy. *Chem. Rev.* **1998**, *98* (4), 1515–1562. https://doi.org/10.1021/cr941195u.

(9) Warneke, J.; Hou, G.-L.; Aprà, E.; Jenne, C.; Yang, Z.; Qin, Z.; Kowalski, K.; Wang, X.-B.; Xantheas, S. S. Electronic Structure and Stability of $[B_{12}X_{12}]^{2-}$ (X = F–At): A Combined Photoelectron Spectroscopic and Theoretical Study. *J. Am. Chem. Soc.* **2017**, *139* (41), 14749–14756. https://doi.org/10.1021/jacs.7b08598.

(10) Strauss, S. H. The Search for Larger and More Weakly Coordinating Anions. *Chem. Rev.* **1993**, *93* (3), 927–942. https://doi.org/10.1021/cr00019a005.

(11) Boldyrev, A. I.; Gutowski, M.; Simons, J. Small Multiply Charged Anions as Building Blocks in Chemistry. *Acc. Chem. Res.* **1996**, *29* (10), 497–502. https://doi.org/10.1021/ar960147o.

(12) Blades, A. T.; Kebarle, P. Study of the Stability and Hydration of Doubly Charged Ions in the Gas Phase: SO_4^{2-}, $S_2O_6^{2-}$, $S_2O_8^{2-}$, and Some Related Species. *J. Am. Chem. Soc.* **1994**, *116* (23), 10761–10766. https://doi.org/10.1021/ja00102a046.

(13) De Vlugt, I. J. S.; Lecours, M. J.; Carr, P. J. J.; Anwar, A.; Marta, R. A.; Fillion, E.; Steinmetz, V.; Hopkins, W. S. Infrared-Driven Charge-Transfer in Transition Metal-Containing $B_{12}X_{12}^{2-}$ (X = H, F) Clusters. *J. Phys. Chem. A* **2018**, *122* (35), 7051–7061. https://doi.org/10.1021/acs.jpca.8b05750.

(14) Boeré, R. T.; Derendorf, J.; Jenne, C.; Kacprzak, S.; Keßler, M.; Riebau, R.; Riedel, S.; Roemmele, T. L.; Rühle, M.; Scherer, H.; Vent-Schmidt, T.; Warneke, J.; Weber, S. On the Oxidation of the Three-Dimensional Aromatics [B12X12]2− (X=F, Cl, Br, I). *Chem. – Eur. J.* **2014**, *20* (15), 4447–4459. https://doi.org/10.1002/chem.201304405.

(15) Hopkins, W. S.; Carr, P. J. J.; Huang, D.; Bishop, K. P.; Burt, M.; McMahon, T. B.; Steinmetz, V.; Fillion, E. Infrared-Driven Charge Transfer in Transition Metal $B_{12}F_{12}$ Clusters. *J. Phys. Chem. A* **2015**, *119* (31), 8469–8475. https://doi.org/10.1021/acs.jpca.5b03932.

(16) Lecours, M. J.; Marta, R. A.; Steinmetz, V.; Keddie, N.; Fillion, E.; O'Hagan, D.; McMahon, T. B.; Hopkins, W. S. Interaction of $B_{12}F_{12}^{2-}$ with All- *Cis* 1,2,3,4,5,6 Hexafluorocyclohexane in the Gas Phase. *J. Phys. Chem. Lett.* **2017**, *8* (1), 109–113. https://doi.org/10.1021/acs.jpclett.6b02629.

(17) Carr, P. J. J.; Warneke, J.; Featherstone, J.; Jenne, C.; Loire, E.; Hopkins, W. S. The Structure of Proton-Bound Triethylammonia (X = F, Cl) Clusters. *Mol. Phys.* **2019**, *117* (21), 2972–2979. https://doi.org/10.1080/00268976.2019.1595203.

(18) Warneke, J.; Jenne, C.; Bernarding, J.; Azov, V. A.; Plaumann, M. Evidence for an Intrinsic Binding Force between Dodecaborate Dianions and Receptors with Hydrophobic Binding Pockets. *Chem. Commun.* **2016**, *52* (37), 6300–6303. https://doi.org/10.1039/C6CC01233G.

(19) Warneke, J.; Dülcks, T.; Knapp, C.; Gabel, D. Collision-Induced Gas-Phase Reactions of Perhalogenated Closo-Dodecaborate Clusters – a Comparative Study. *Phys. Chem. Chem. Phys.* **2011**, *13* (13), 5712. https://doi.org/10.1039/c0cp02386h.

(20) Warneke, J.; Wang, X.-B. Measuring Electronic Structure of Multiply Charged Anions to Understand Their Chemistry: A Case Study on Gaseous Polyhedral Closo-Borate Dianions. *J. Phys. Chem. A* **2021**, *125* (31), 6653–6661. https://doi.org/10.1021/acs.jpca.1c04618.

(21) Wöhner, K.; Wulf, T.; Vankova, N.; Heine, T. Strong Binding of Noble Gases to $[B_{12}X_{11}]^-$: A Theoretical Study. *J. Phys. Chem. A* **2021**, *125* (22), 4760–4765. https://doi.org/10.1021/acs.jpca.1c01909.

(22) Gabelica, V.; Shvartsburg, A. A.; Afonso, C.; Barran, P.; Benesch, J. L. P.; Bleiholder, C.; Bowers, M. T.; Bilbao, A.; Bush, M. F.; Campbell, J. L.; Campuzano, I. D. G.; Causon, T.; Clowers, B. H.; Creaser, C. S.; De Pauw, E.; Far, J.; Fernandez-Lima, F.; Fjeldsted, J. C.; Giles, K.; Groessl, M.; Hogan Jr, C. J.; Hann, S.; Kim, H. I.; Kurulugama, R. T.; May, J. C.; McLean, J. A.; Pagel, K.; Richardson, K.; Ridgeway, M. E.; Rosu, F.; Sobott, F.; Thalassinos, K.; Valentine, S. J.; Wyttenbach, T. Recommendations for Reporting Ion Mobility Mass Spectrometry Measurements. *Mass Spectrom. Rev.* **2019**, *38* (3), 291–320. https://doi.org/10.1002/mas.21585.

(23) Ieritano, C.; Yves Le Blanc, J. C.; Schneider, B. B.; Bissonnette, J. R.; Haack, A.; Hopkins, W. S. Protonation-Induced Chirality Drives Separation by Differential Ion Mobility Spectrometry. *Angew. Chem. Int. Ed.* **2022**, *n/a* (n/a), e202116794. https://doi.org/10.1002/anie.202116794.

(24) Campbell, J. L.; Zhu, M.; Hopkins, W. S. Ion-Molecule Clustering in Differential Mobility Spectrometry: Lessons Learned from Tetraalkylammonium Cations and Their Isomers. *J. Am. Soc. Mass Spectrom.* **2014**, *25* (9), 1583–1591. https://doi.org/10.1007/s13361-014-0939-3.

(25) Ieritano, C.; Hopkins, W. S. The Hitchhiker's Guide to Dynamic Ion–Solvent Clustering: Applications in Differential Ion Mobility Spectrometry. *Phys. Chem. Chem. Phys.* **2022**, *24* (35), 20594–20615. https://doi.org/10.1039/D2CP02540J.

(26) Oomens, J.; Sartakov, B. G.; Meijer, G.; Von Helden, G. Gas-Phase Infrared Multiple Photon Dissociation Spectroscopy of Mass-Selected Molecular Ions. *Int. J. Mass Spectrom.* **2006**, *254* (1–2), 1–19. https://doi.org/10.1016/j.ijms.2006.05.009.

(27) Martens, J.; Berden, G.; Gebhardt, C. R.; Oomens, J. Infrared Ion Spectroscopy in a Modified Quadrupole Ion Trap Mass Spectrometer at the FELIX Free Electron Laser Laboratory. *Rev. Sci. Instrum.* **2016**, *87* (10), 103108. https://doi.org/10.1063/1.4964703.

(28) Martens, J.; Van Outersterp, R. E.; Vreeken, R. J.; Cuyckens, F.; Coene, K. L. M.; Engelke, U. F.; Kluijtmans, L. A. J.; Wevers, R. A.; Buydens, L. M. C.; Redlich, B.; Berden, G.; Oomens, J. Infrared Ion Spectroscopy: New Opportunities for Small-Molecule Identification in Mass Spectrometry - A Tutorial Perspective. *Anal. Chim. Acta* **2020**, *1093*, 1–15. https://doi.org/10.1016/j.aca.2019.10.043.

(29) Neese, F.; Wennmohs, F.; Becker, U.; Riplinger, C. The ORCA Quantum Chemistry Program Package. *J. Chem. Phys.* **2020**, *152* (22), 224108. https://doi.org/10.1063/5.0004608.

(30) Pracht, P.; Bohle, F.; Grimme, S. Automated Exploration of the Low-Energy Chemical Space with Fast Quantum Chemical Methods. *Phys. Chem. Chem. Phys.* **2020**, *22* (14), 7169–7192. https://doi.org/10.1039/C9CP06869D.

(31) Chai, J.-D.; Head-Gordon, M. Long-Range Corrected Hybrid Density Functionals with Damped Atom–Atom Dispersion Corrections. *Phys. Chem. Chem. Phys.* **2008**, *10* (44), 6615. https://doi.org/10.1039/b810189b.

(32) Weigend, F.; Ahlrichs, R. Balanced Basis Sets of Split Valence, Triple Zeta Valence and Quadruple Zeta Valence Quality for H to Rn: Design and Assessment of Accuracy. *Phys. Chem. Chem. Phys.* **2005**, *7* (18), 3297. https://doi.org/10.1039/b508541a.

(33) Carr, P. J. J. Computational and Spectroscopic Investigations of Intermolecular Interactions in Clusters, University of Waterloo, 2019. http://hdl.handle.net/10012/14890 (accessed 2024-10-31).

(34) Rohdenburg, M.; Mayer, M.; Grellmann, M.; Jenne, C.; Borrmann, T.; Kleemiss, F.; Azov, V. A.; Asmis, K. R.; Grabowsky, S.; Warneke, J. Superelectrophilic Behavior of an Anion Demonstrated by the Spontaneous Binding of Noble Gases to [B12Cl11]−. *Angew. Chem. Int. Ed.* **2017**, *56* (27), 7980–7985. https://doi.org/10.1002/anie.201702237.

(35) Haack, A.; Ieritano, C.; Hopkins, W. S. MobCal-MPI 2.0: An Accurate and Parallelized Package for Calculating Field-Dependent Collision Cross Sections and Ion Mobilities. *The Analyst* **2023**, *148* (14), 3257–3273. https://doi.org/10.1039/D3AN00545C.

(36) Anwar, A.; Psutka, J.; Walker, S. W. C.; Dieckmann, T.; Janizewski, J. S.; Larry Campbell, J.; Scott Hopkins, W. Separating and Probing Tautomers of Protonated Nucleobases Using Differential Mobility Spectrometry. *Int. J. Mass Spectrom.* **2018**, *429*, 174–181. https://doi.org/10.1016/j.ijms.2017.08.008.

(37) Campbell, M. T.; Glish, G. L. Fragmentation in the Ion Transfer Optics after Differential Ion Mobility Spectrometry Produces Multiple Artifact Monomer Peaks. *Int. J. Mass Spectrom.* **2018**, *425*, 47–54. https://doi.org/10.1016/j.ijms.2018.01.007.

(38) Atkins, C. G.; Rajabi, K.; Gillis, E. A. L.; Fridgen, T. D. Infrared Multiple Photon Dissociation Spectra of Proton- and Sodium Ion-Bound Glycine Dimers in the N−H and O−H Stretching Region. *J. Phys. Chem. A* **2008**, *112* (41), 10220–10225. https://doi.org/10.1021/jp805514b.

(39) Ung, H. U.; Moehlig, A. R.; Khodagholian, S.; Berden, G.; Oomens, J.; Morton, T. H. Proton-Bridge Motions in Amine Conjugate Acid Ions Having Intramolecular Hydrogen Bonds to Hydroxyl and Amine Groups. *J. Phys. Chem. A* **2013**, *117* (6), 1360–1369. https://doi.org/10.1021/jp311506y.

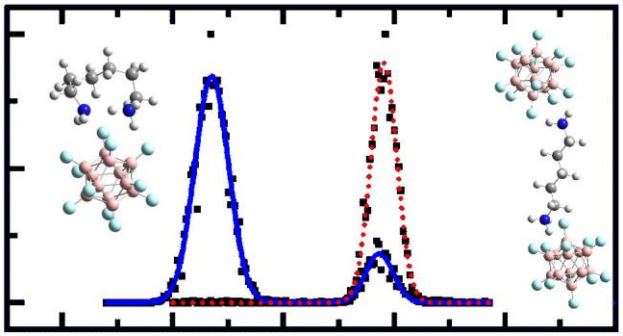

For ToC graphic